Wind barriers optimization for minimizing collector mirror soiling in a parabolic trough collector plant.

M.A. Moghimi[1,*], G. Ahmadi[2]

[1]*Lecturer,Clean Energy Research Group, Department of Mechanical and Aeronautical Engineering, University of Pretoria, Pretoria, South Africa.*

[2] *Professor, Department of Mechanical and Aeronautical Engineering, Clarkson University, Potsdam, NY 13699-5725, USA*

[*]Corresponding author: mohammad.moghimiardekani@up.ac.za, moghimi64@gmail.com

Abstract:

Wind barriers, according to their sizes and shapes, can effectively control, shift and even modify the airflow field in their downstream. These structures can accelerate the wind flow over the mirror field and move the airborne particles away from the mirrors. For example, in concentrated solar power plants it is highly desirable to engineer the system in a way that fewer particles are deposited within the solar field, in particular, onto mirror surfaces. Therefore, design optimization of dust barriers could significantly impact the mirror soiling and favourably reduce the cleaning water consumption of a solar power plant. This study focuses on the optimization of a solid wind barrier around a parabolic trough collector plant for their protection against dust soiling. The presented simulation results show that an optimum solid wind barrier is able to direct large amount of particles (in this study, more than 86%) to pass over the solar field with very small fraction (around 0.8%) being deposited on the mirrors. In addition, it was found that the barrier wall is more effective in deflecting the larger particles from the solar field.

Keywords: Wind barrier, Mirror soiling, Computational fluid dynamics, Optimization, Parabolic Trough Collector, Atmospheric Boundary Layer, Particle deposition, Turbulent, Discrete Phase Method.

1. Introduction:

Concentrated solar power (CSP) is a type of solar technology which focuses the impinging solar rays onto reflector surfaces (Heliostats/ mirrors), which eventually transfers the sun energy to a working fluid for generating power. The most developed form of CSP plants is the parabolic trough collectors (PTC), which is the most mature CSP technology. In 2016, Chaanaoui et al. [1] analysed the information of world operational installed capacity of CSP plants which were publicly available in literature. They reported that 3.5 GW out of 4.2 GW operational installed CSP plants are PTC.

Therefore, improving the performance of PTC plants is one of the interesting topics in the field of CSP and is widely discussed in literatures. Researchers' approaches in tackling this issue are focusing on enhancement of either thermal or optical performance of receivers. Regarding with thermal performance improvement, adding nano-particles to conventional Heat Transfer Fluid (HTF) of PTC plants [2-5] and placing insert-in heat transfer enhancer in the absorber tube receiver (metal foam [6], porous disk [7], perforated plate [8], helical fins [9], rectangular longitudinal fins [10]) are among the recent approaches suggested in literature. Regarding with optical performance improvement of PTCs, researchers mainly focus on reducing cosine loss in the system. Their approaches to tackle this issue are tilting receiver in the conventional single axis tracking PTC plants [11-15], or using two-axis tracking system for PTCs [16-19] and some novel ideas like PTC plant with rotatable axis tracking [20]. As one may note, the suggested approaches are mostly in the early stage of R&D (research and development) and requires long track of investigations to be approved by industry and be implemented in the PTC plants. The state of the art of this study, is presenting an effective practical and easy-implemented approach to improve the performance of current PTC plants as proven technology. This approach must be as simple as possible that not even the future plants consider it in their design but the operational ones can utilize it. Therefore, this study looks at the performance improvement of PTC plants from a different view angle.

In practice, the performance of PTC plant depends on the high reflectivity of mirror surfaces and in particular their surface cleanness (avoiding mirror soiling). According to Niknia et al. [21], 1.5 g/m^2 dust deposition can reduce the instantaneous and average performance of the PTC plant, respectively by 60% and 37%. Therefore, controling mirror soiling can be an interesting attributor in the performance improvement of a PTC plant.

In the conventional PTC plants mirror are regularly cleaned to keep the plant performance in acceptable range. The most effective mirror cleaning systems use 0.2-1 litres of water per square meters of collector areas. This is relatively high level of water consumption especially for desert areas that are perfect locations for CSP plant due to high DNI (Direct Normal Irradiance) and available number of sunny days, but with little precipitations. For example, in the PTC project of NOOR I, in Morocco, each individual mirror is washed every seven days and more than 36.5 million litres of demineralized water are consumed every year [22]. In addition, the plants in desert-like regions are exposed to frequent dust storms and sand depositions which require more often mirror cleaning schedules. Table 1 lists some global CSP regions of interest and shows how harsh those regions could be for a CSP plant in terms of annual fallen dust rate, which eventually ends up as dust deposition.

Table 1: Fallen dust rates for various CSP plants [23].

Country	Location	Fallen dust [tons/km^2/year]
Iraq	Khur Al-Zubir	75.92
Iraq	Um Qasir	193.47
Oman	Al-Fahal	89
Saudi	Arabia Riyadh	392
Palestine	Dead Sea	45

Chad	North Dianena	142
Nigeria	Kano	137-181
Greece	Crete	10-100
USA	Arizona	54
USA	Nevada	4.3-15.7
USA	California	6.8-33.9
Libya	Libya	155
Morocco	Tan Tan	175
Morocco	Boujdour	219
Mauritania	Dakhla	191
Mali	Niger river	913-10446
Australia	Namoi valley	16.9-58.2
China	Shapotou	372

Commercially, mirrors of PTC plants are washed with one or several of the following systems: mechanically controlled high-pressure jet washing, mechanically controlled brush washing, deluge style washing, manual brush washing, manual high-pressure jet washing and robot washing [24]. However, these methods require significant amount of water for washing mirror surfaces. Therefore, researchers came up with various chemical or mechanical ideas to save water consumption for mirror cleaning in CSP plants. These include, anti-soiling coating, paved roads instead of dirt roads in plants, stowing the mirrors in storm, electrostatic repulsion of mirrors, mirror shaker (a mechanical vibrator which shakes off accumulated dusts on mirrors) and erection of wind barrier [22].

One of the simplest and economical approaches for reducing mirror soiling is the optimal design of wind barriers. For security reasons PTC plants are usually enclosed with wire mesh fences. However in sandy places like deserts, the fences are replaced by solid walls so that they can act as wind barrier and dust protection as well. However, studies on the effects of wind barriers on the aerodynamic loads and/or particle deposition in the PTC field are rather scarce [25, 26]. Presence of a wind barrier causes the formation of a separation bubble that deflects the wind to flow above the mirror field and consequently, move the airborne particles to a height so that they deposit beyond the solar field. That is the barrier creates a sheltering effect for the solar mirror field. Therefore, according to their dimensions, shapes and designs, the wind barriers can effectively control, shift and even modify the wind flow pattern downstream and impact the particle deposition on mirrors. To the best of authors' knowledge, there is no comprehensive study on optimization of wind barriers for controlling particle deposition in PTC fields.

In this work the effects of the presence of a solid wind barrier equipped with flap at the tip on the wind flow field as well as the transport and deposition of particle are studied using a computational modelling approach. Simulations were performed for a range of barrier heights, flap angles and sizes. It was shown that an appropriately designed barrier can reduce the particle deposition in the solar field. Particular attention was given to the optimization of the wind barrier in order to engineer the airborne fate over a solar field and minimizing the number of particles fall within the field, in particular being deposited onto mirror surfaces.

2. Computational domain, fluid flow and problem formulation:

2.1. Problem Layout

Fig.1 shows the schematic sketch of the investigated PTC field. The field includes six trough receivers with fixed mirror pitch and aperture. To minimize mirror soiling in the field a wind barrier is placed in the direction of the prevailing wind. The barrier includes a solid wall and an inclined flap at its tip. The barrier is erected in a certain distance from the first mirror surface (the leftmost curved surface in Fig.1). Finding optimum barrier specifications is the goal of this study. These specifications include barrier height, flap length, flap angle and barrier distance from the first collector which are respectively annotated as l_2, l_3, θ and l_1 in Fig. 1.

For this study, the length and the height of the computational domain were set, respectively, as 62.5 m and 20 m. To accurately capture the realistic and physical conditions of the prevailing wind, the fully developed atmospheric boundary layer (ABL) profiles were imposed on the inlet of the computational domain which will be discussed in more details in the following section.

2.2. Fluid flow and particle conditions

To accurately model particle depositions on the mirrors of PTC field, the airflow and particle transport and deposition need to be properly modelled. Attentions need to be given to the prevailing wind inlet condition and the particle interactions with mirror surfaces. Here a fully developed atmospheric boundary layer (ABL) profiles was used for the inlet wind velocity and an approximation for particle deposition on the mirror surface is described.
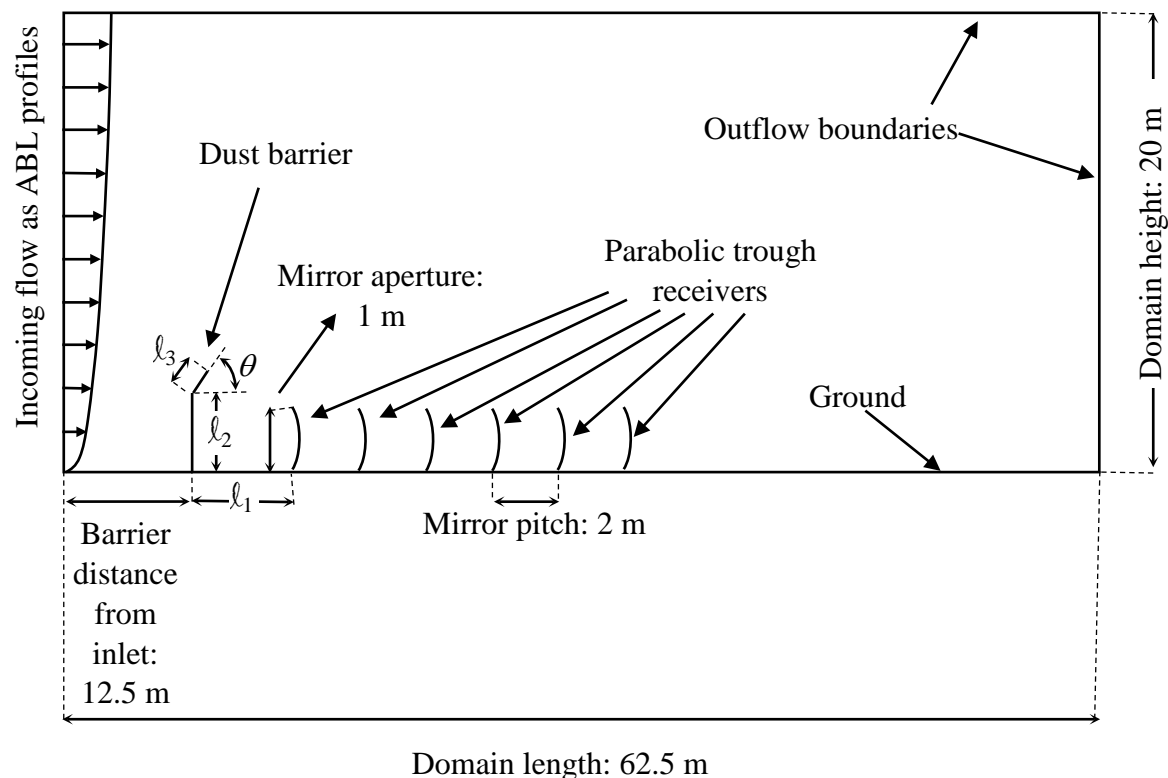

Domain length: 62.5 m

Fig. 1: Schematic sketch of the proposed PTC field and with wind barrier.

4

2.2.1. Atmospheric boundary layer (ABL) profiles

Since the PTC field is exposed to an atmospheric wind, use of the correct model of the inlet mean flow velocity and turbulence intensity profiles is just as critical as accurate modelling of the geometric feature of the computational domain. Here the fully-developed atmospheric boundary layer (ABL) profile is used. This will allow using a short distance upstream of the PTC field rather to introduce the infinitely large terrain upstream, that saves the computational efforts. However, it is crucial to have sufficient space before the wind barrier; otherwise, due to blockage effect the simulation over predicts the results. Good practice rules in CFD recommend the minimal distance of any object from the inlet surface to be about 5 times the dimension of the object. Therefore, in this study, a distance of 12.5 m was introduced between the wind barrier and the inlet to computational domain to obtain physically realistic results (Fig. 1).

To have successful CFD simulations in an atmospheric computational domain, there should be no difference (almost negligible difference) between the inlet profile and the incident profile (the profile obtained in an equivalent but empty domain at the model position). According to Blocken, et al. [27] minor changes in incident profiles may lead to significant changes in flow field. Therefore, in computational wind engineers a horizontally homogenous ABL is defined when the inlet (approach airflow toward the model) and incident flow profiles in a similar but an empty computational domain match. Indeed, the ABL profiles are selected such that they are analytical solutions of the k-epsilon transport equations. Therefore, by implementing these ABL profiles, they would be consistently preserved when travelling in an empty domain.

According to Richard and Norris [28], the only acceptable profiles for horizontal homogenous boundary layer are:

$$U(y) = \frac{u^*_{ABL}}{\kappa} ln\left(\frac{y}{y_0}\right); \ where \ u^*_{ABL} = \frac{U_{ref}}{\kappa} ln\left(\frac{y_{ref}}{y_0}\right) \tag{1}$$

$$k = \frac{{u^*_{ABL}}^2}{\sqrt{C_\mu}}; \ where \ u^*_{ABL} = \frac{U_{ref}}{\kappa} ln\left(\frac{y_{ref}}{y_0}\right) \tag{2}$$

$$\varepsilon = \frac{{u^*_{ABL}}^3}{\kappa y}; \ where \ u^*_{ABL} = \frac{U_{ref}}{\kappa} ln\left(\frac{y_{ref}}{y_0}\right) \tag{3}$$

where $U(y)$, u^*_{ABL}, κ, C_μ, y_{ref}, and y_0, respectively, are mean-stream-wise velocity component, ABL friction velocity, von Karman constant, turbulence model constant, reference height, and aerodynamic roughness length.

According to Blocken, et al. [27] to maintain a horizontally homogeneous ABL flow simulation in a computational domain, an equivalent wall shear stress of the ABL profiles has to be imposed on the upstream and downstream region of the domain. The associated wall shear stress of ABL is:

$$\tau_w = \rho(u^*_{ABL})^2 \tag{4}$$

By implementing the above mentioned profiles one can simulate horizontally homogeneous ABL flow. The turbulence intensity profile is defined as,

$$I_u(y) = \frac{\sqrt{\frac{2}{3}k}}{U(y)} \tag{5}$$

The turbulence intensity profile is also checked for inlet, approach and incident flow in the empty domain to provide assurance of a horizontal homogeneous ABL condition.

2.2.2. Partial deposition in a CSP field

In general, particles impinging onto a surface may be bounced off, stick or even erode the solid surface. The particle adhesion that causes particle deposition on a surface is the main interest of this study. Therefore, before performing particle simulation study, the question that how a particle stick to a glass surface (mirror in this study) after collision must be examined.

According to [29-30], particle adhesion to a glass surface is a function of three main parameters: 1. Local climate (e.g., wind speed and direction, and relative humidity …). 2. Dust properties (size, shape, angularity, composition, and hardness). 3. Surface properties (glass material, surface roughness, and glass surface energy). The behaviour of real particles in wind and sandstorms is a complex phenomenon. Therefore, in this study, only the particle size and the wind velocity are considered as the main particle adhesion parameters and, the rest of the aforementioned parameters are assumed to be constant.

According to Lee et al. [31] sand grains in the size range of 2.5μm to 10μm become airborne in wind gusts of about 15-17m/sec. Bagold [32] showed that airborne sand particles of 25-250μm in diameter would have a Stokes velocity less than 10m/sec. (The Stokes velocities for 25μm and 250μm droplets are, respectively, 0.02m/s and 2m/s.). In addition, Sansom et al. [26] reported that there is a little evidence for large particle depositions (>250 μm) on CSP mirror fields. These observations comply with the airborne particle size distributions in PTC sites in Iran and Spain. Dust particle sampling pole in a PTC plant in Shiraz, Iran shows that large particles (>500 μm) are mainly found at the ground level and not at heights above 0.5 m while smaller particles (<200 μm) are found at height 1 m (See Fig. 2). Full size inspection of PTC mirror facets on test lines at the CIEMAT Plataforma Solar de Almeria (PSA) in Spain shows only small particles (<250 μm) deposited on the mirror facets (Sansom et al [33]).
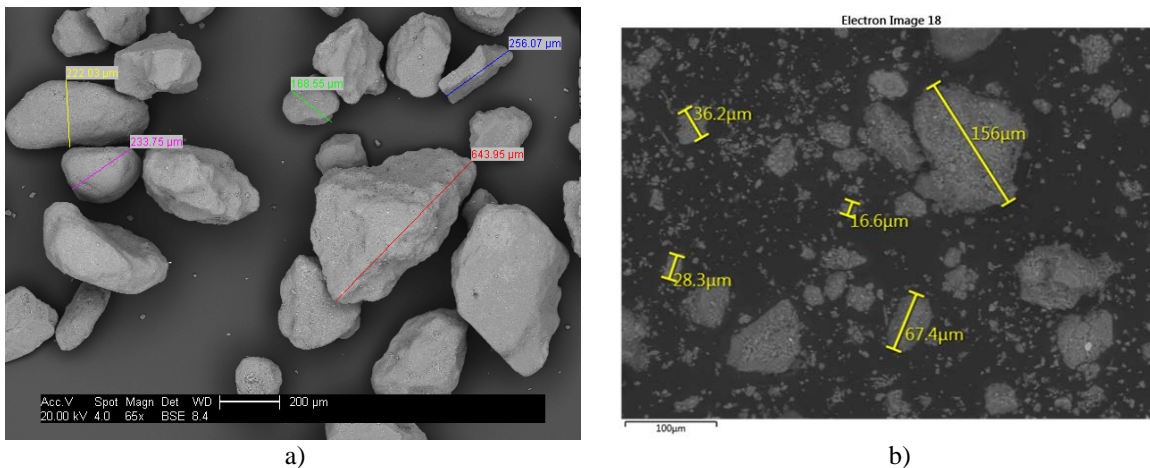

Fig 2. Particle collected from particle pole collector in Iran CSP plant at a) ground level, b) 1m above the ground. Pictures were reprinted from Sansom et al. [33].

Therefore, as a rule of thumb, the fates of particle collisions with mirror facets in CSP plants can be assumed as:

At low impact velocity (< 10 m/s), large particles (>250 µm) are reflected from surface.
At impact velocity (~ 10 m/s), small particles (<250 µm) adheres onto the surface.
At impact velocity (~ 10 m/s), large particles (>250 µm) erodes the surface.

These assumptions are made based on the above discussions and Fig. 3, which was presented by Kilnkov et al. [34] in their review of literature on impact of particles onto plane solid surfaces.

Fig. 3: Classification of particle impact on solid surface as reported in the literature. The picture is reprinted from Kilnkov et al. [34].

2.3. Optimization problem

As noted before, the geometrical parameters of the studied PTC field including the associated geometric constraints are shown in Fig. 1. These geometrical constrains are the mirror aperture, the mirror pitch, and the height and length of the computational domain. The other geometrical parameters (barrier height, flap length, flap angle and barrier distance from the first collector) shown in Fig. 1, form design variable set considered in the optimization. These parameters and the associated bounds on various parameters used in the optimization are tabulated in Table 1. These bounds were defined based on the practical concerns in design and construction of wind barriers.

Table 1: Definition of objective and parameter ranges.

Independent Parameter	Lower Bound	Upper Bound
Barrier distance from the first mirror (l_1) [m]	0.5	3.5
Barrier height (l_2) [m]	0.5	2.5
Flap length (l_3) [m]	0.05	0.5
Flap angle (θ) [°]	5	175

The optimization problem is formulated as follow

$$Minimize\{Number\ of\ trapped\ particles\ as\ function\ of\ (\tilde{x})\}$$

with $\tilde{x} = (l_1, l_2, l_3, \theta)$ subject to bounds on , design variable set $\tilde{x}$ as listed in Table 1. In essence, this optimization formulation finds the best configuration of the dust barrier for minimum number of particles that are deposited onto the mirror facets.

3. Methodology

3.1. Introduction

3.1.1. CFD method: assumption, governing equations, material and boundary conditions

To simulate the airflow and particle trajectories in the PTC field, an Eulerian-Lagrangian approach is used. The continuous airflow field is first evaluated using the Eulerian approach and the Lagrangian particle trajectories are computed by solving the particle equation of motion. That is, the discrete phase model (DPM) under the assumption of one-way coupling, which can be used for dilute concentrations. Indeed in one-way coupling simulations, the fluid phase carries the particulate, but the influence of particles on the flow field, which is negligiblely small for dilute system, is ignored. In this study, the simulation is using the ANSYS Fluent (version 18.1) code under the following assumptions.

3.1.1.1. Continuous phase (ABL flow)

It is assumed that the airflow is a two dimensional field and is under steady state condition. For ABL flows it is reasonable to treat air as an incompressible fluid due to low speeds. Therefore, the constant properties of air at 300K (constant temperature) are used in the simulations. No-slip velocity boundary conditions for are imposed at all solid surfaces including barrier and mirror walls. (To maintain homogeneity of the ABL in the computational domain wall shear stress (Eq. 4) is imposed on the ground (bottom side of the domain in Fig. 1). As discussed earlier, fully developed ABL velocity, k and ε profiles are imposed at the inlet of the domain, and outflow boundary conditions are implemented on the top and right sides of the domain (please consult Fig. 1). Also the wind average velocity at the inlet ABL velocity profile was set at 10 m/s to simulate the particle adhesion assumption discussed in section 2.2.2.

As discussed earlier for the airflow simulations the Reynolds Averaged Navier Stokes (RANS) is used in these simulations. In addition, the realizable k-ε turbulence model was in the analysis to account for effects of wind flow turbulence. The corresponding governing equations are [35]:

$$\frac{\partial}{\partial x_i}(\rho u_i) = 0 \tag{6}$$

$$\frac{\partial}{\partial x_i}(\rho u_i u_j) = -\frac{\partial p}{\partial x_i} + \frac{\partial}{\partial x_j}\left[\mu\left(\frac{\partial u_i}{\partial x_j} + \frac{\partial u_j}{\partial x_i} - \frac{2}{3}\delta_{ij}\frac{\partial u_l}{\partial x_l}\right)\right] + \frac{\partial}{\partial x_j}\left(-\rho\overline{u_i' u_j'}\right) \tag{7}$$

$$\frac{\partial}{\partial x_i}(\rho k u_j) = \frac{\partial}{\partial x_j}\left[\left(\mu + \rho C_\mu \frac{k^2}{\varepsilon}\right)\frac{\partial k}{\partial x_j}\right] - \rho\varepsilon - \rho\overline{u_i' u_j'}\frac{\partial u_i}{\partial x_j} \tag{8}$$

$$\frac{\partial}{\partial x_i}(\rho\varepsilon u_j) = \frac{\partial}{\partial x_j}\left[\left(\mu + \rho C_\mu \frac{k^2}{1.2\varepsilon}\right)\frac{\partial \varepsilon}{\partial x_j}\right] + \rho\varepsilon C_1\left(\frac{\partial u_i}{\partial x_j} + \frac{\partial u_j}{\partial x_i}\right) - 1.2\,\rho\frac{\varepsilon^2}{k + \sqrt{v\varepsilon}} \tag{9}$$

where x, ρ, μ, p, u, u', k, ε are, respectively, position vector, fluid density, fluid viscosity, mean fluid pressure, mean fluid velocity vector, fluctuating velocity vector, turbulence kinetic energy and dissipation rate of turbulence energy. Indices *i, j, l* annotate the components of a vector. In addition, C_1 is a function of mean strain and turbulence field (k and ε) while C_μ is a function of rotation rate, mean strain, the system rotation angular velocity and turbulence field.

3.1.1.2. Particulate Phase (airborne particles)

The sand particles were released at the height of 0.5 to 3 m at the inlet of the domains. This injection includes 2000 sand particles as a group injection with particle diameters in range of 25 to 250 µm. The particle size distribution was defined based on Rosin-Rammeler diameter distribution method. The sand particles were chosen as inert particles with density of 1350 kg/m^3 [36]. The spherical drag force on particles was considered which assumes the particles are smooth spheres. Therefore, the equivalent diameter spherical particles were used in the simulation (Please see Fig. 2-b for sample of gathered data at a CSP site). Turbulent dispersion of particles was simulated by the stochastic discrete random walk model. Turbulent dispersion occurs due to velocity fluctuations in the flow and need to be included in the simulation to account for the important effects of turbulence dispersion [37]. To generate statistically meaningful results for discrete random walk tracking, each injection is tracked 10 times. The last but not least, the boundary conditions of the domain were set as follow: the inlet and outflow boundaries were set as "escape" while the ground, mirror and barrier surfaces were set as "trap" conditions.

Based on the above assumptions, the particle trajectory is calculated by integrating the particle force balance equation, in a Lagrangian reference frame. That is:

$$\frac{du_i^p}{dt} = F_D(u_i - u_i^p) - g_i(\rho_p - \rho)/\rho_p \tag{10}$$

where u_i^p, u_i, F_D, g_i, ρ_p and ρ, respectively are velocity vector of particle, instantaneous velocity vector of the fluid, drag coefficient, acceleration of gravity, particle density and the fluid density.

3.1.2. Mesh generation

The meshing Package of ANSYS WB 18.1 was used to generate mesh in this optimization study. To capture boundary layer properly, 7 layer of inflation were generated next to solid wall boundaries in the computational domain. To generate the most smooth and mapped mesh in the entire computational domain following approaches were used. First the computational domain was sliced by two planes (a vertical plane 19 m from barrier and a horizontal plane 4 m above the ground) to have 4 zones which three of them were far from any objects (mirror field or barrier). These three zones have a biased mapped mesh towards the ground and the domain inlet and their mesh generations were controlled with edge sizing. The mesh of the last zone (the zone includes mirror field and barrier, bottom left zone see Fig.4 a) was controlled by automatic settings to have an almost smooth and mapped mesh.

The computational domain was generated using the parameters introduced in Fig. 1 and Table 1. The aforementioned settings were used to create the computational mesh in the domain. As it was reported by ANSYS, the average of the element quality and orthogonal quality of this case were 0.80263 and 0.98885, respectively, where 1 is the perfect quality. This proves the generated mesh in the entire domain is almost mapped uniform mesh. Fig. 4a displays the generated mesh in the computational domain where the plain black region in this figure, is due to high density of mesh elements in that region. To have a clear view of the generated mesh a zoomed-in picture of the mesh is illustrated in Fig. 4b.
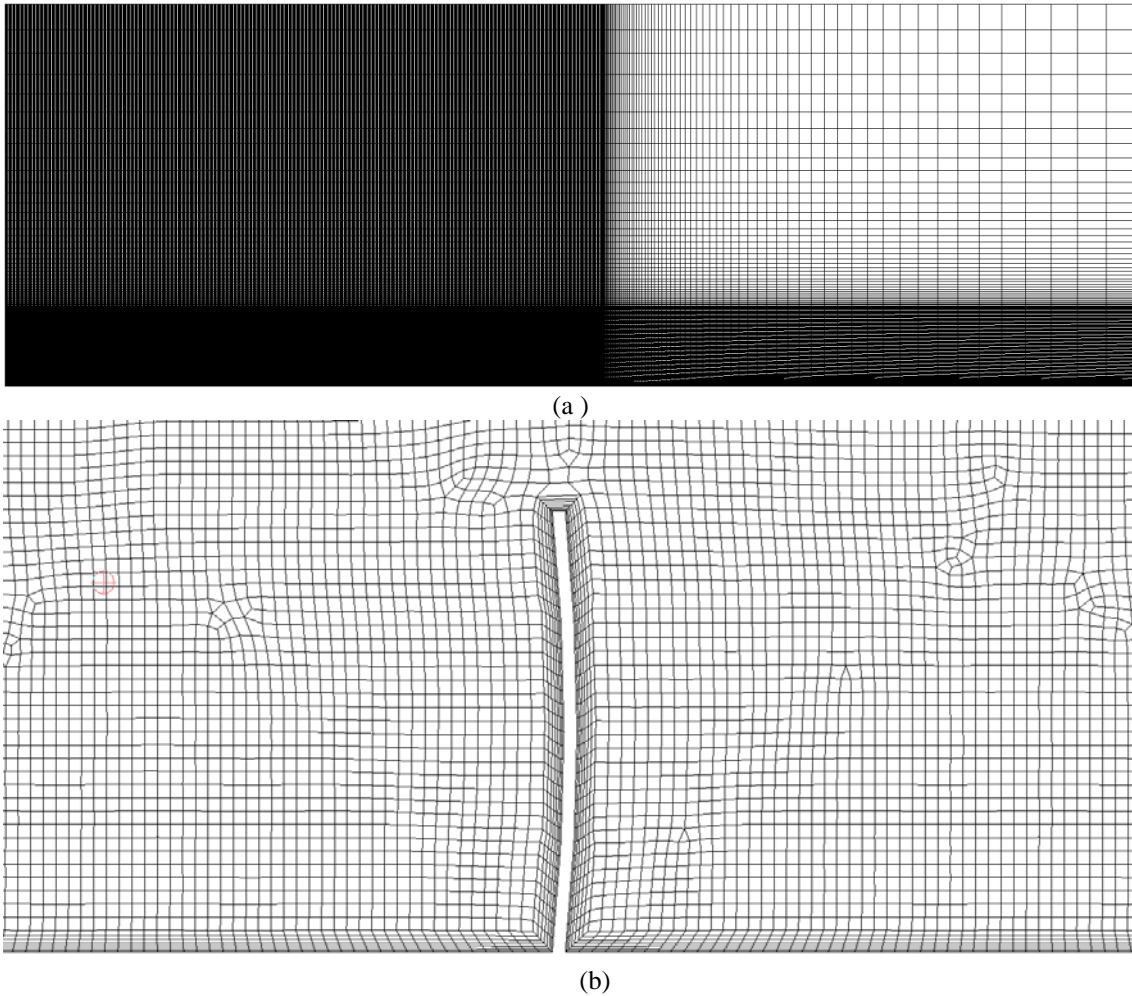
(a)

(b)

Fig. 4. (a) Generated computational mesh on a sample domain. The biased mapped mesh (toward the ground, bottom wall, and the inlet, the left wall) is depicted in the top right zone of this figure. b) Zoomed-in mesh on the sample domain. The 7 layers of inflation around the solid walls and the ground were shown in this figure.

3.1.3. CFD settings

The steady state turbulent fluid flow in the domain was solved using the Fluent solver module of ANSYS. After getting converged solution for the fluid flow in the domain, the DPM model was activated and solved under that assumption of the one way coupling approach. The CFD setting strategy included solving the governing equations using SIMPLE algorithm for the first 10000 iterations and then switching on the Pressure-Based Coupled Solver with Pseudo-Transient activation for pressure-velocity coupling and solving 10000 iterations. This switching was implemented to increase the stability and quicker convergence of solution for all the cases that may face problematic convergence, due to occurrence of unsteady phenomena, such as vortex shedding. Then, the DPM settings were activated in the entire domain. This setting strategy led to convergence of all 25 optimization case studies, which will be discussed in the subsequent sections. The reported results of optimization obtained after about 5 days of running simulations on 10 cores of an Intel Xeon CPU E5-2630 v4 with 16 GB RAM. The numbers of generated cells on the 25 case studies vary from 242,486 to 283,540 elements.

3.2. Optimization method (algorithm and model setting)

For this optimization study ANSYS DX (DesignXplorer) was used. ANSYS DX is a mathematical optimization which is based on Response Surface Method. To construct the response surfaces, design of experiments (DOE) must be performed to generate design points. In this study, 25 auto-defined Central Composite Design were determined for 4 defined independent parameters. Each of those samples was run individually and the corresponding information of the objective (summation of particle depositions on mirror facets) was extracted for each case. A 2nd order polynomial response surface with variable variation type was then constructed for the output parameters and then combined. The determinations of the optimum location of these surfaces (candidate points) were performed by using two different approaches: 1) MOGA and 2) screening followed by NLPQL. The former approach, MOGA, is a based on the Fast and Elitist evolutionary algorithm: NSGA-II (Non-dominated Stored genetic algorithm-II). The second approach begins with screening method, which is a non-iterative direct sampling method based on Hammersley algorithm. This method determines the starting values (initial guesses) for the following method, NLPQL. NLPQL or NonLinear Programming by Quadratic Lagrangian is a mathematical optimization algorithm which generates a new candidate set based on the provided initial guesses (candidate points of screening method). Indeed NLPQL is the complementary of screening method and provides a more redefined approach than the screening alone.

The settings of the first optimization approach (the MOGA method) were: 100 for both "Number of Initial Samples" and "Number of Samples per Iterations", 80, 0.5 and 20 for "Maximum allowable Pareto Percentage", "Convergence Stability Percentage" and "Maximum Number of Iterations", respectively. This means the optimization process terminates when the resulting front of the MOGA contains at least 80 points (80% of Number of Samples per Iterations) or reaches the maximum number of iterations, whichever is reached sooner.

The settings of the second optimization approach (Screening followed by NLPQL) were as follow: the Screeing method settings were set on the default values while the NLPQL method settings were "Central", 1e-6 and 20 for "Finite Difference Approximation", "Allowable Convergence" and "Maximum Number of Iterations", respectively. Similar to MOGA the optimization process terminates whenever either the allowable convergence or the maximum number of iterations is reached.

For more information on the design point generations, optimization approaches, meaning of these optimization settings and in general optimization process in ANSYS DX, please consult ANSYS DX help [37] or Moghimi et al. papers [38-39].

4. Results & discussions

4.1. Validations

One of the important features that must be verified in the study is checking the ABL to see if it is horizontally homogenous. Therefore as discussed earlier, the empty computational domain (domain with no mirror field and wind barrier) is considered for this study. The dimensions of the domain as well as the boundary conditions used are shown in Fig. 1 and section 3.1.1.1. Indeed horizontal homogeneity of an ABL verifies that the incident profile seen by the wind barrier in the study is the same as the one generated at the inlet. As displayed in Figure 5a and b, both the mean velocity and turbulence intensity profiles

preserve their shape and order from inlet to outlet. The profiles are at the inlet, 0.5 m, 1.5 m, 2.5 m, 3.5 m and 5 m away from the inlet as well as at the outlet. Therefore, ABL profile of this study can be considered horizontally homogenous, with the slight decay across the domain.
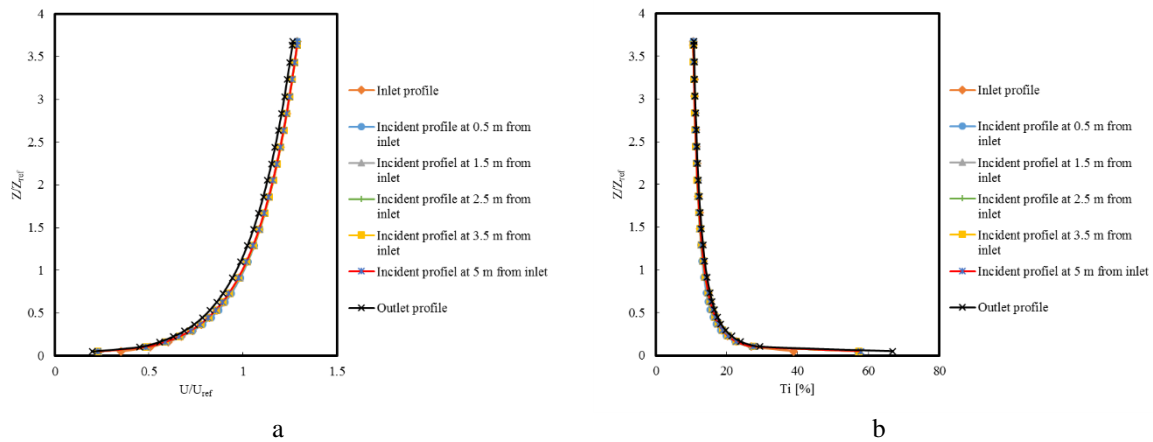

Fig 5. Verifying horizontal homogeneity of the ABL. a) Dimensionless velocity profile b) Turbulence intensity.

Furthermore, to validate the 2D numerical approach used in this study, a PTC experimental setup presented by Paetzold et al. [40] was modelled. The setup had dimensions of 500, 150, 40 and 40 mm, respectively, for aperture, focal length, tube absorber diameter and rotating tube diameter. According to [40], during the experiment a slight negative pitch of the trough of 1–2° was observed, due to the non-rigid turntable of the wind tunnel. Therefore, a 2D trough with a pitch angle of -2° was set in the empty computational domain displayed in Fig. 1 and the wind flow around the trough was simulated using with the noted boundary conditions described in section 3.1.1.1. In the study of Paetzold et al. [40], there were some missing information such as roughness of rotating tube, collector and absorber tube, and or the distance of rotating tube from the collector and the ground. Therefore, in the present CFD simulation, a few assumptions consistent with the available information were made. Fig. 6 compares the predicted u-velocity contours with the PIV data of [40].

It is seen that the CFD velocity contour shows an acceptable agreement with the PIV data. By comparing Figs. 6b, 6c and 6d, one finds that the flow separation at the leading edge of trough is well predicted by the model. This flow separation forms a shear layer between the slightly upward accelerated flow and the low speed flow inside the trough as a recirculation region is generated. Underneath the collector, according to the CFD result (Fig. 6c and 6d) the flow is accelerated between the rotating tube and the trough. However it seems in the experiment, the flow is attached longer and also has a longer horizontal wake extension than CFD simulation.   These differences may be attributed to the variation of surface roughness of rotating tube and back of the reflector in the simulation compared to the physical setup. It should be emphasized that this comparison is mainly based on the circular region shown in Fig 6b, while the parts of flow separation and wake formation occurred in the shaded area of the PIV result. The verifications shown in Fig. 6 show the applicability of the modelling approach for investigating the effects of wind barrier on soiling of PTCs.
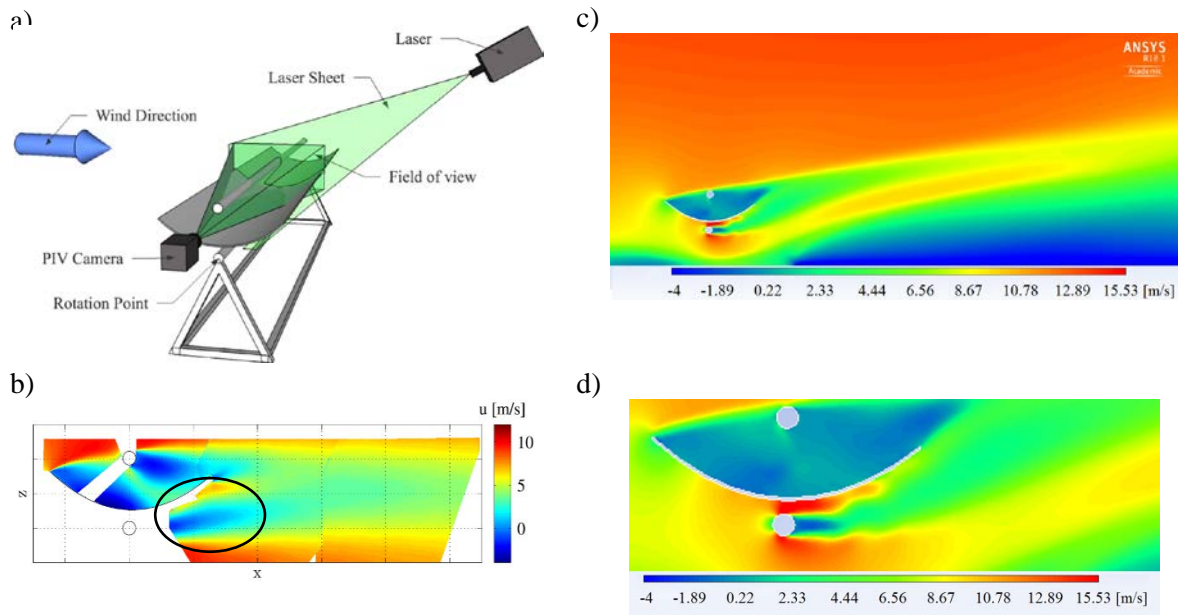
Fig 6. Comparison of predicted u-velocity contours with the experimental data of [40]. a) Schematic of the PTC experimental PIV set-up in the wind tunnel. b) The experimental PIV results (white areas in PIV results did not have data) at nominal pitch angle= 0°. c) The CFD simulation at pitch angle= -2°. d) The zoomed-in simulation around the collector. Pictures a) and b) were reprinted from [40].

4.2. Optimization results

The response surfaces of the optimization problem (the wind barrier optimization of the PTC field) were generated based on non-parametric regression which leads to the best goodness of fit for this problem. This goodness of fit of the response surfaces predicted by this method versus actual calculated sampling data (design points) is shown in Fig. 7. This goodness of fit was reported from ANSYS DX. As displayed, this method generates a response surface with an acceptable accuracy that can be utilized for the optimization process.
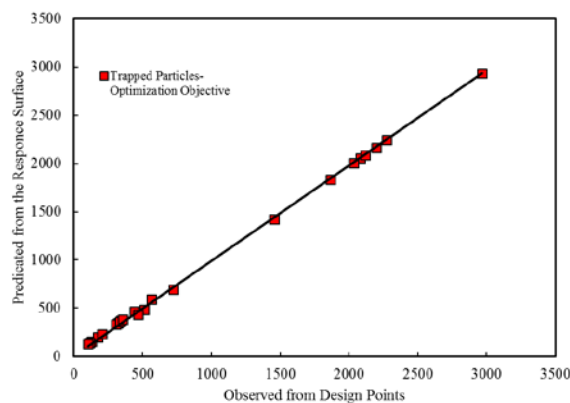
Fig. 7. Goodness of Fit

The optimization on the generated response surfaces converged after 823 iterations for MOGA approach and 1000 and 823 iterations for screening and NLPQL approaches, respectively. The local sensitivity of the objective (trapped particles on mirror facets) in the response surface for particular values of independent parameters is shown in Fig. 8.

13

According to this figure, the most effective parameters are the barrier height and flap length which could favourably impact on the amount of the deposited airborne on the mirror facets.
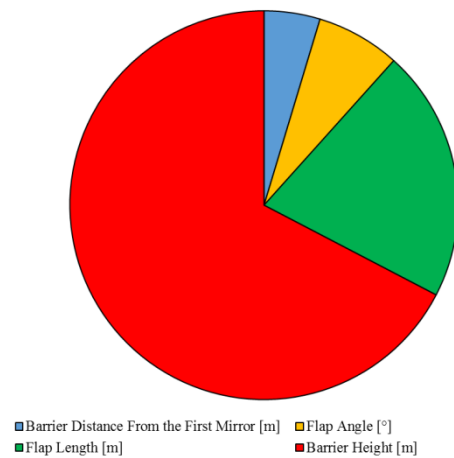

Fig. 8. Local sensitivity of the optimization objectives vs. independent parameters at a local point in the generated response surfaces. The local points were picked at the values of screening and NLPQL 2nd candidate listed in Table 2.

To show the effect of every two independent parameters on the objective of the optimization problem, two response surfaces are displayed in Fig. 9. It is noticed that the response surface variations based on barrier height and flap length are much sharper than that for flap angle and barrier distance. This observation is consistent with the optimization sensitivity of independent parameters shown in Fig 8. Fig. 9a shows there is an optimum distance for constructing barrier from the mirror field to decrease particle deposition on the mirror surface. In addition, taller barriers have favourable effect until an optimum height and then it has a negative effect that increases particle deposition on the mirrors. This trend is due to the fact that until an optimum height, there is sheltering effect because of accelerating airflow over the barrier but beyond the optimum height the turbulence gets stronger in the separation bubble and creates a steep return of the displacement flow toward the mirror field. In addition, flap construction on the tip of the barriers has interesting effects on the boosting or degradation of vortices downstream. As it is shown in Fig. 9b there are optimum points for the flap characteristics (both height and angle) which end to a concave upward surface. The combination of these two parameters could impact the formation of vortices downstream which eventually affects particle deposition on the mirror field.
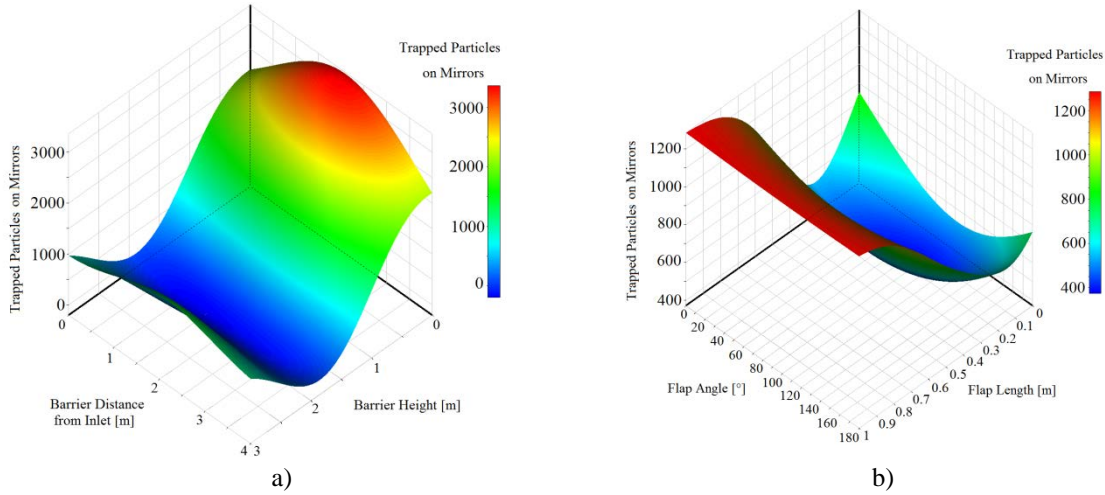
Fig. 9. 3D response surface of objective (z-axis) versus independent parameters: a) Barrier height (x-axis) and barrier distance from the first mirror (y-axis). b) Flap length (x-axis) and flap height (y-axis).

Values for three utopian points were automatically selected by ANSYS DesignXplorer among all feasible Pareto optimal cases. These values for each optimization approaches are summarized in Table 2. The optimal set of parameters (optimum results) obtained in response surface optimization approaches, were fed into the CFD model to calculate the actual results of trapped particles (particle depositing onto mirror surfaces). These actual results were listed for objective in Table 2.

Table 2: Candidate utopian points

Parameters (unit)	MOGA approach			Screening and NLPQL approaches		
	1st candidate	2nd candidate	3rd candidate	1st candidate	2nd candidate	3rd candidate
Barrier distance from the first mirror (l_1) [m]	2.802	1.962	1.028	0.811	0.781	3.076
Barrier height (l_2) [m]	1.838	1.824	1.884	1.765	1.989	1.849
Flap length (l_3) [m]	0.344	0.327	0.303	0.286	0.119	0.141
Flap angle (θ) [°]	105	14	155	158	129	65
Objective	**Calculated**	**Calculated**	**Calculated**	**Calculated**	**Calculated**	**Calculated**
Trapped Particles	212	228	195	206	178	235

The results show that both approaches introduce candidate points that lead to roughly similar results for the objective. However, screening and NLPQL approaches have a slightly better predication of utopian candidates in comparison with MOGA. These results can be attributed to of the nature of MOGA technique which has been developed for multi-objective optimization.

The results shows the optimization process tends to make l_2 and l_3, respectively, between 1.7-2 m and 0.12-0.35 m. In contrast to these independent parameters, l_1 and θ have wider utopian ranges roughly between 0.8-2.8 m and 14 to 158 °, respectively. These narrow and wide utopian ranges can be justified due to the optimization sensitivity to independent parameters as shown in Fig. 8. Parameters with higher sensitivities lead to narrow utopian ranges while less sensitive parameters lead to wider utopian ranges.

For further investigations, the 2nd candidate of the screening and NLPQL approaches is selected for tracking 5,000,000 particles in the domain. The detailed CFD results for this candidate are displayed in Fig. 10. For a clear vision on the particle trajectories, in figures 10 and 11, only 400 particle trajectories are displayed. As discussed earlier, the average wind

velocity across the profile at the inlet is 10 m/s. Fig. 10a displays, the flow streamlines coloured by velocity magnitude and Fig. 10b displays the particle trajectories coloured by particle diameters. It is seen that the barrier and the flap create an upward stream where the airflow is accelerated, from about 9.2 m/s at the tip of barrier to 12.3 m/s over the mirror field (yellow to red region in Fig. 10a). As displayed in Fig. 10b some smaller particles (below 100 to 150 µm diameter) disperse by the turbulence fluctuations and are more prone to be captured by the recirculating region of the airflow beyond the wind barrier where a few are eventually deposited in the mirror field (see Fig. 11 a and b as well). In addition the smaller particles are carried to further distances by the accelerated mean airflow over the mirror field before due to their weight their trajectories deflect and they either fall on the ground or escape from the computational domain. Hence, their residence times in the computational domain are much more than large particles because the further distances they travel (see Fig. 11 a-d as well). These behaviours are attributed to the low mass (low inertia) of small particles.

Although due to the formation of the recirculation region downstream of the barrier from 5,000,000 tracked particles, less than 14% of particles (less than 691,000) enter into the mirror field, only 41,399 particles are trapped on mirror facets, and the others are eventually deposited on the ground within the solar field. Table 3 summarizes the fate of particles in the domain. It is seen that almost 2/3 of particles are trapped in the computational domain (3,440,563from 5,000,000 tracked particles). Interestingly about 80% of those trapped particles (2,749,991 from 3,440,563 particles) are deposited outside of the mirror field (either before the barrier or after the last mirror). In other words, more than 86% of tracked particles (4,309,428 particles) were not fallen in the mirror field domain. It is seen that about 0.8% of released particles (41,399 out of 5,000,000 particles) deposit onto the front side of mirrors. This proves the successful design of barrier which could hugely reduce the water consumption of a plant for mirror cleaning. Another interesting observation that can decrease the required water for a plant mirror cleaning is the pattern of mirror washing in a mirror field. Although this suggestion is out of the scope of the present work, however it can be considered by future researchers for further investigations. As listed in Table 3, 3,697 and 3,962 particle are respecticly deposited on the 1st and the 2nd mirrors, while 6,265, 7,730, 9,777 and 9,968 particles are deposited, respectively, on the 3rd, 4th, 5th and 6th mirrors. Therefore, one can conclude that for regular mirror washing schedule of a PTC plant with a barrier wall, the first two rows closer to the barrier may require less washing than the other rows. However, to be able to draw a definite conclusion, the simulations should be performed with much larger number of particles in order to decrease statistical uncertainties.

To provide a wider picture of transport and deposition of particles of different sizes, a set of complimentary studies were performed. Here, instead of releasing particles with a distribution of sizes, ensemble of particles with the same diameter was realised at the distance of 2 m before the barrier at the height of 0.5-3 m. The corresponding trajectories coloured by particle residence time are reported in Fig. 11a-d for 25 µm, 100 µm, 180 µm and 250 µm particles. It is seen that smaller particles (25 µm) are more prone to be captured by the recirculation region behind the barrier wall. This is because the inertial of these particles are low and they are more easily deflected by turbulence fluctuations and enter into the vertical flow region, some of which will be eventually deposited on the mirror field (see Fig. 11 a and b). In addition, smaller particles are accelerated by the mean airflow over the wind barrier

and travel further distance which consequently fall further away in the computational domain
due to their inertia.   For example, the accelerated particles by means of airflow over the wind
barrier in case of 25 µm, 100 µm, 180 µm and 250 µm can respectively reach to 15.3 m, 11
m, 7.8 m and 6.4 m height from the ground before due to their weigh deflect their trajectories
and either fall on the ground or escape the domain (see Fig. 11 a-d) . Moreover, as shown in
the zoomed-in pictures of Figures 11, larger particles are deposited more before wind barrier
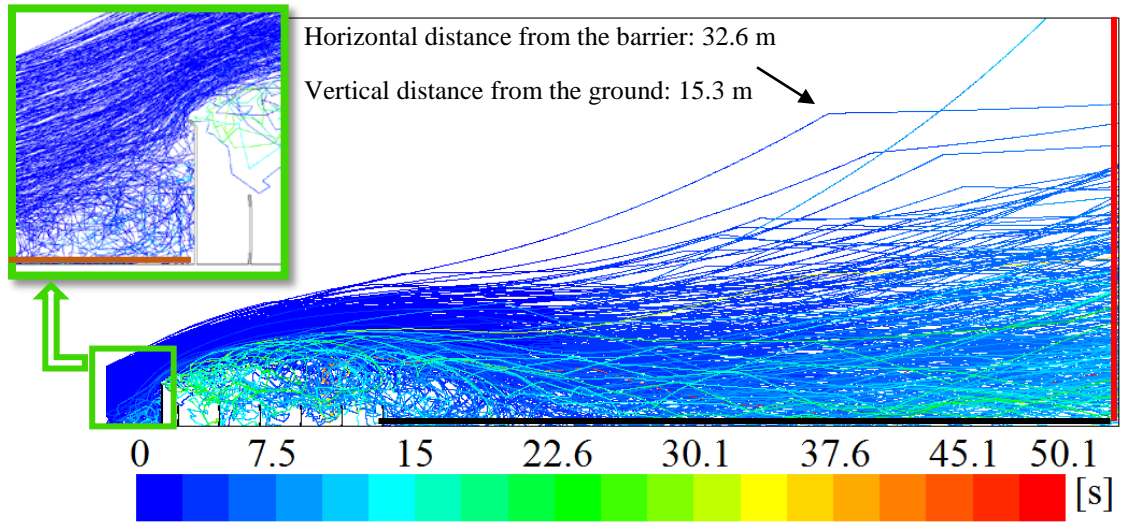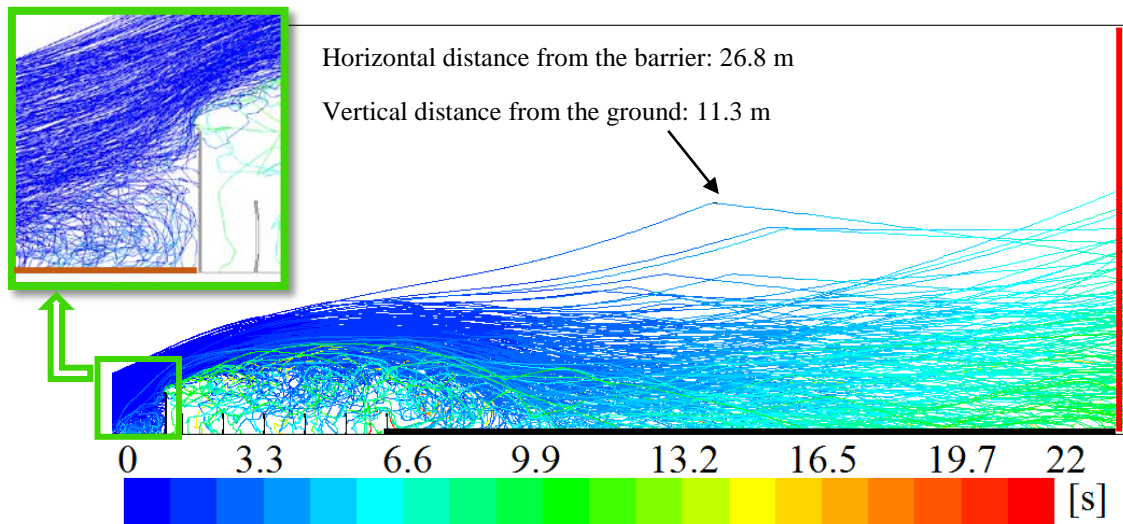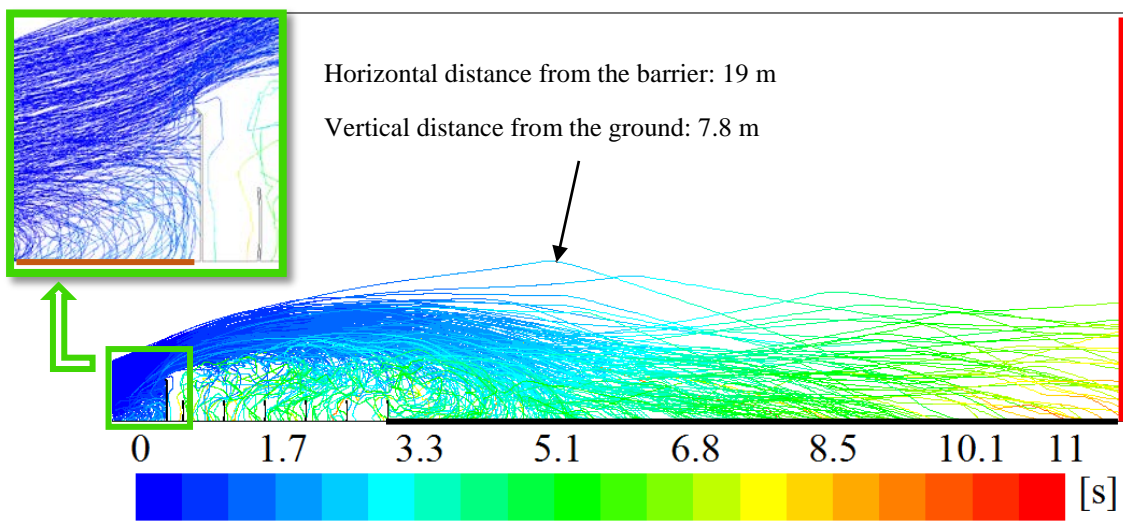due their high inertia.

a)

b)
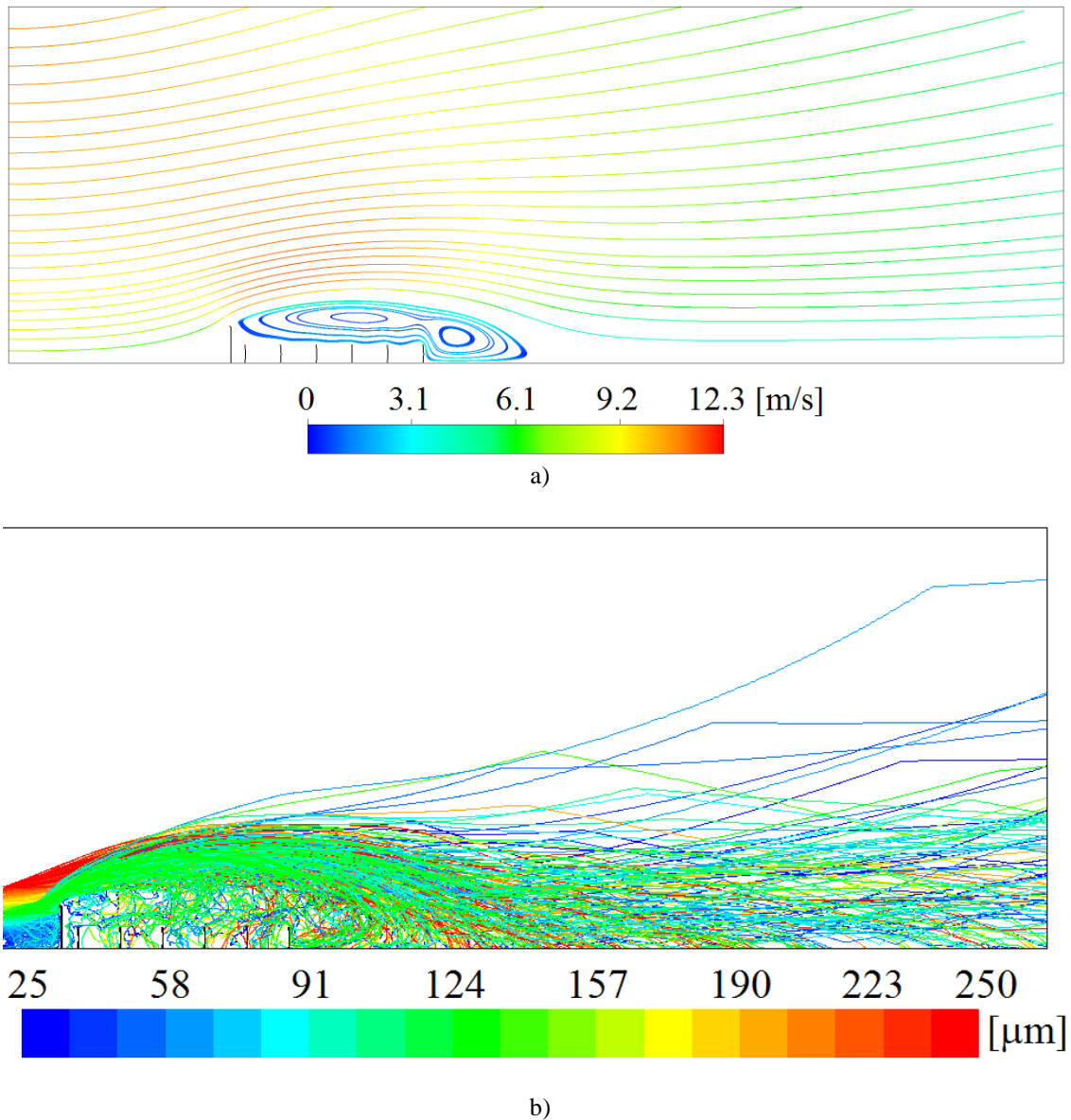
Fig. 10. CFD results of the screening and NLPQL 2nd candidate. a) Streamlines coloured by velocity magnitude. b)
Zoomed-in 400 particle trajectories coloured by particle size.

Horizontal distance from the barrier: 32.6 m

Vertical distance from the ground: 15.3 m

a)

Horizontal distance from the barrier: 26.8 m

Vertical distance from the ground: 11.3 m

b)

Horizontal distance from the barrier: 19 m

Vertical distance from the ground: 7.8 m

c)

18

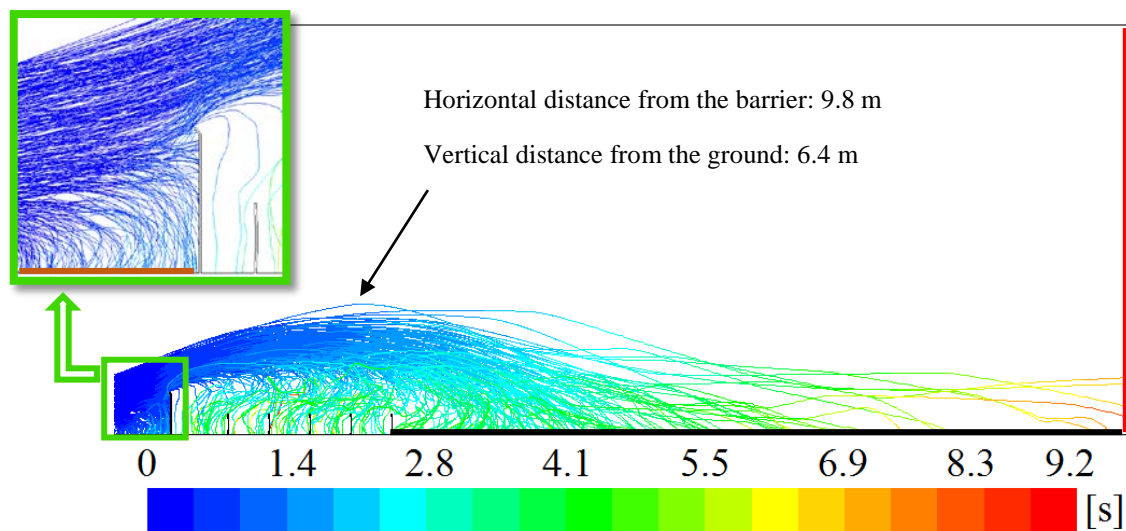Horizontal distance from the barrier: 9.8 m

Vertical distance from the ground: 6.4 m

d)

Fig. 11. 400 particle trajectories of single particle diameter coloured by particle residence time over the field as well as zoom-in trajectories before wind barrier.
a) 25 µm; where out of 400 tracked particles, 147 and 115 particles are respectively deposited after mirror field (thick black line) and before barrier (thick brown line) and 4 particles are escaped from domain (thick red line).
b) 100 µm; where out of 400 tracked particles, 194 and 82 particles are respectively deposited after mirror field (thick black line) and before barrier (thick brown line) and 28 particles are escaped from domain (thick red line).
c) 180 µm; where out of 400 tracked particles, 145 and 54 particles are respectively deposited after mirror field (thick black line) and before barrier (thick brown line) and 148 particles are escaped from domain (thick red line).
d) 250 µm; where out of 400 tracked particles, 45 and 26 particles are respectively deposited after mirror field (thick black line) and before barrier (thick brown line) and 306 particles are escaped from domain (thick red line).

Table 3: Particle fates in the domain of the screening and NLPQL 2nd candidate for 5,000,000 tracked particles. The minimum, maximum and mean diameter of the particles respectively are 25, 250 and 150 µm.

Breakdown list of particle fates	
Number of particles escaped from the 1st outflow boundary (Vertical boundary right at the end of computational domain)	1,554,818
Number of particles escaped from the 2nd outflow boundary (Horizontal boundary at the top side of the computational domain)	4,619
Number of particles fall on the ground before barrier (The ground between inlet and barrier)	326,406
Number of particles fall on the ground between barrier and the first mirror	27,025
Number of particles fall on the ground in the mirror field (The ground includes mirror pitches)	492,073
Number of particles fall on the ground after the mirror field (The ground between the last mirror and outlet)	2,185,401
Number of particles fall on the 1st mirror facet-front side (the mirrors are counted from the leftmost one)	3,697
Number of particles fall on the 2nd mirror facet-front side	3,962
Number of particles fall on the 3rd mirror facet-front side	6,265
Number of particles fall on the 4th mirror facet-front side	7,730
Number of particles fall on the 5th mirror facet-front side	9,777
Number of particles fall on the 6th mirror facet-front side	9,968
Number of particles fall on back side of all the mirrors	130,075
Number of particles fall on the barrier and flap surfaces	23,8184
Summary	
Total number of particles tracked in the domain where particles are realised from the inlet	5,000,000
Total number of particles escaped from the domain	1,559,437
Total number of particles trapped in the domain	3,440,563

Total number of particles fall in the mirror field (i.e. between the barrier and the last mirror which includes back and front of mirror facets as well as the ground between barrier and 1st mirror, and the grounds between mirrors)	690,572
Total number of particles fall out of mirror filed (i.e. the ground before the barrier, the ground after the last mirror and the barrier itself)	2,749,991

The presented results show that wind barrier could provide a simple, effective and practical approach for lowering the amount of water consumption for mirror washing in PTC plants or in general any CSP plants. Thus, this method could lower the Levelized Cost of Electricity (LCOE) by decreasing the expenses for mirror cleaning. Based on the CSP plant condition and prevailing wind, the presented method can be used for optimization of dust barriers at different plants around the globe to significantly cuts down the required water consumption.

5. Conclusions

In this study a mathematical optimization approach was used and the optimal wind barrier for a parabolic trough collector plant was developed. The optimal design of the barrier minimized the soiling of PTC mirror field. This study was carried out using the ANSYS-Fluent code for the CFD simulations as well as the Response Surface Method optimization approach.

The specific conclusions of the present study are:

1. The CFD provides an economical approach for simulating the effect of wind barriers on flow and particle transport around solar power plant mirror field. In particular, with appropriate design of the barrier the amount of particle deposition on the mirrors can be significantly reduced.
2. An optimally designed solid wind barrier can direct huge amount of particles (more than 86%) away over the solar field and reduce the dust deposition on the mirror facets field to very small amount (around 0.8%).
3. Optimization of wind barrier is a simple, effective and practical approach for significantly reducing water consumption of concentrating solar power plants, as well as, Photovoltaic plants. This will lead to lowering the plant operation cost and the cost of electricity production.
4. This study can be used as a user guide for future research for simulating, optimizing and for design of novel wind barrier for concentrating solar power plants.

References:

[1] Chaanaoui M, Vaudreuil S, Bounahmidi T, Benchmark of Concentrating Solar Power plants: historical, current and future technical and economic development. Procedia Computer Science 2016; 83: 782-89.

[2] Colangelo G, Favale E, de Risi A, Laforgia D. Results of experimental investigations on the heat conductivity of nanofluids based on diathermic oil for high temperature applications. Appl Energy 2012; 97: 828-33.

[3] Bellos E, Tzivanidis C, Antonopoulos KA, Gkinis G. Thermal enhancement of solar parabolic trough collectors by using nanofluids and converging-diverging absorber tube. Renew Energy 2016; 94: 213-22.

[4] Mwesigye A, Huan Z, Meyer JP. Thermodynamic optimisation of the performance of a parabolic trough receiver using synthetic oil–Al2O3 nanofluid. Appl Energy 2015; 156: 398-412.

[5] Mwesigye A, Meyer JP. Optimal thermal and thermodynamic performance of a solar parabolic trough receiver with different nanofluids and at different concentration ratios. Appl Energy 2017; 193: 393-413.

[6] Wang P, Liu DY, Xu C. Numerical study of heat transfer enhancement in the receiver tube of direct steam generation with parabolic trough by inserting metal foams. Appl Energy 2013; 102: 449–60.

[7] Ravi Kumar K, Reddy KS. Thermal analysis of solar parabolic trough with porous disc receiver. Appl Energy 2009; 86: 1804-12.

[8] Mwesigye A, Bello-Ochende T, Meyer JP. Heat transfer and thermodynamic performance of a parabolic trough receiver with centrally placed perforated plate inserts. Appl Energy 2014; 136: 989-1003.

[9] Muñoz J, Abánades A. Analysis of internal helically finned tubes for parabolic trough design by CFD tools. Appl Energy 2011; 88: 4139–49.

[10] Bellos E, Tzivanidis C, Tsimpoukis D. Multi-criteria evaluation of parabolic trough collector with internally finned absorbers. Appl Energy 2017; 205: 540-61.

[11] Donald R. Solar energy. New Jersey: Prentice Hall; 1981.

[12] El-Kassaby M. Prediction of optimum tilt angle for parabolic trough with the long axis in the north-south direction. Sol Energy 1994;16:99–109.

[13] Zhang Y., Qiu Z, Li P., et al. Calculating the optimum tilt angle for parabolic solar trough concentrator with the north-south tilt tracking mode. In: 2013 fourth international conference on digital manufacturing & automation. p. 329–34.

[14] David LW. Effect of manual tilt adjustments on incident irradiation on fixed and tracking solar panel. Appl Energy 2011;88:1710–9.

[15] Markus E, Wolf-Dieter S, Jurgen R. Maximum temperature difference in horizontal and tilted absorber pipes with direct steam generation. Energy 2004;29:665–76.

[16] Fernández-García A, Zarza E, Valenzuela L, et al. Parabolic-trough solar collectors and their applications. Renew Sustain Energy Rev 2010;14:1695–721.

[17] National Renewable Energy Laboratory. Concentrating solar power: large payload solar tracker. <https://www.nrel.gov/csp/facilities.html#lpst>.

[18] Bakos George C. Design and construction of a two-axis Sun tracking system for parabolic trough collector (PTC) efficiency improvement. Renew Energy 2006;31:2411–21.

[19] Al-Soud Mohammed S, Abdallah Essam, Akayleh Ali, et al. A parabolic solar cooker with automatic two axes sun tracking system. Appl Energy 2010;87:463–70.

[20] Qu W, Wang R, Hong H, Sun J, Jin H. Test of a solar parabolic trough collector with rotatable axis tracking, Appl Energy 2010; 207: 7-17.

[21] Niknia I, Yaghoubi M, Hessami R, A novel experimental method to find dust deposition effect on the performance of parabolic trough solar collectors, International Journal of Environmental Studies, 2012. DOI:10.1080/00207233.2012.664810

[22] Bouhafra O, Optimization of cleaning strategy project Noor I, Al akhawayn University, 2017, Capstone final report. Available at: http://www.aui.ma/sse-capstone-repository/pdf/spring-2017/OPTIMIZATION%20OF%20CLEANING%20STRATEGY%20PROJECT_NOOR%20I.pdf

[23] Sansom C, Comley P, King P, Almond H, Atkinson C, Endaya E, Predicting the effects of sand erosion on collector surfaces in CSP plants, Energy Procedia 2015; 69 : 198-207.

[24] Yu S, Guan Z, Gurgenci H, Collinsville Solar Thermal Project: Solar Mirror Cleaning Requirements, 2017, RATCH-Australia Corporation. report available at:

http://ratchaustralia.com/collinsville/docs/Collinsville%20Solar%20Thermal%20Feasibility%20Study%20-%20Solar%20Mirror%20Cleaning.pdf

[25] Torres García E, Ogueta-Gutiérrez M, Ávila S, Franchini S, Herrera E, Meseguer J, On the effects of windbreaks on the aerodynamic loads over parabolic solar troughs, Applied Energy 2014; 115: 293-300.

[26] Sansom C, King P, Fernández-García A, Almond H, Kayani T, Boujjat H, The design of dust barriers to reduce collector mirror soiling in CSP plants, SolarPACES 2017, Santigo, Chile.

[27] Blocken B, Stathopoulos T, Carmeliet J, CFD simulation of the atmospheric boundary layer: wall function problems. Atmospheric environment 2007; 41: 238-252.

[28] Richards PJ, Norris SE, Appropriate boundary conditions for computational wind engineering models revisited. Journal of Wind Engineering and Industrial Aerodynamics 2011; 99: 257-266.

[29] Li A, Ahmadi G, Bayer RG, Gaynes MA, Aerosol particle deposition in an obstructed turbulent duct flow. Journal of Aerosol Science, 25 (1994) 91 -112.

[30] Jiang Y, Lu L, Ferro AR, Ahmadi G, Analyzing wind cleaning process on the accumulated dust on solar photovoltaic (PV) modules on flat surfaces. Solar Energy, http://dx.doi.org/10.1016/j.solener.2017.08.083.

[31] Lee JA, Gill TE, Mulligan KR, Acosta MD, Perez A.E, Land use/land cover and point sources of the 15 December 2003 dust storm in southwestern North America, Geomorphology 2009; 105: 18-27.

[32] Bagnold R, The physics of blown sand and desert dust, Methuen and Co. Ltd. London (1965).

[33] Sansom C, Almond H, King P, Endaya E, Bouaichaoui S, Airborne Sand and Dust Soiling of Solar Collecting Mirrors, AIP Conference Proceeding 2017; 1850: 130011-1130011-6; doi: 10.1063/1.4984505.

[34] Klinkov SV, Kosarev VF, Rein M, Cold spray deposition: Significance of particle impact phenomena. Aerosopace Science and Technology 2005; 9: 582-91.

[35] Ansys Fluent Help, version 18.1, ANSYS Incorporated (2018).

[36] Nyembwe K, Mashila M, van Tonder PJM, de Beer DJ, Gonya E, physical properties of sand parts produced using a voxeljet vx1000 three-dimensional printer, South African Journal of Industrial Engineering 2016; 27: 136-142.

[37] Tian L, Ahmadi G, Particle deposition in turbulent duct flows comparisons of different model predictions, Journal of Aerosol Science 2007; 38 : 377-97.

[38] Design Exploration User Guide, version 18.1, ANSYS Incorporated (2018).

[39] Moghimi MA, Craig KJ, Meyer JP, Simulation-based optimisation of a linear Fresnel collector mirror field and receiver for optical, thermal and economic performance, Solar Energy 2017; 153: 655–678.

[40] Moghimi MA, Craig KJ, Meyer JP, Optimization of a trapezoidal cavity absorber for the Linear Fresnel Reflector. Solar Energy 2015; 119: 343–361.

[41] Paetzold J, Cochard S,Vassallo A, Fletcher DF, Wind engineering analysis of parabolic trough solar collectors: The effects of varying the trough depth, Journal of Wind Engineering and Industrial Aerodynamics 2014; 135: 118-28.